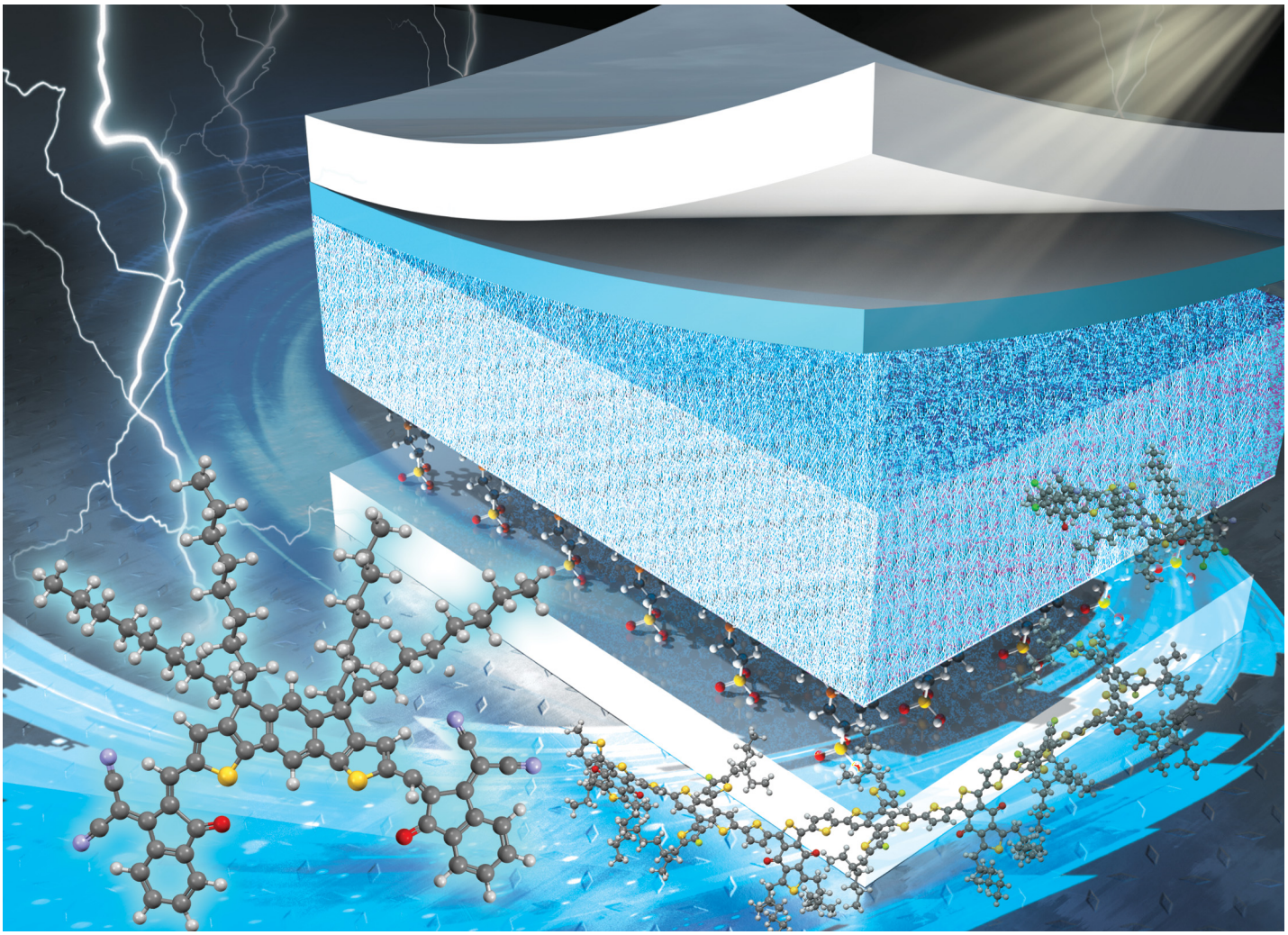

Showcasing research from Professor Hu Chen's laboratory, School of Physical Sciences, Great Bay University, Dongguan, 523000, China.

A 19% efficient and stable organic photovoltaic device enabled by a guest nonfullerene acceptor with fibril-like morphology

Prof. Hu Chen with co-workers reported a nonfullerene acceptor isoIDITC, exhibiting fibril-like morphology, boosts power conversion efficiency to 19% in ternary PM6:BTP-eC9:isoIDITC OPV devices, with enhanced crystallization and carrier mobility, and suppressed recombination. The acceptor's low surface energy and high T_g also suppress demixing and increase device lifetime from 101 to 254 hours. Fibril-like morphology and high T_g make isoIDITC an important third component for stable and high-performance OPVs.

As featured in:

See Yuanbao Lin *et al.*, *Energy Environ. Sci.*, 2023, **16**, 1062.

ROYAL SOCIETY OF CHEMISTRY

rsc.li/ees

Registered charity number: 207890

Energy & Environmental Science

ROYAL SOCIETY OF CHEMISTRY

PAPER

View Article Online
View Journal | View Issue

Cite this: *Energy Environ. Sci.*, 2023, **16**, 1062

A 19% efficient and stable organic photovoltaic device enabled by a guest nonfullerene acceptor with fibril-like morphology†

Hu Chen,[ab] Sang Young Jeong,[c] Junfu Tian,[d] Yadong Zhang,[e] Dipti R. Naphade,[b] Maryam Alsufyani,[d] Weimin Zhang,[b] Sophie Griggs,[d] Hanlin Hu,[f] Stephen Barlow,[e] Han Young Woo,[c] Seth R Marder,[e] Thomas D. Anthopoulos,[b] Iain McCulloch[bd] and Yuanbao Lin *[bd]

A nonfullerene acceptor, isoIDITC, capable of exhibiting fibril-like morphology, is utilized as a third component in organic photovoltaic devices (OPVs). A power conversion efficiency (PCE) of 19% is achieved in ternary PM6:BTP-eC9:isoIDITC bulk-heterojunction (BHJ) devices. Analyses reveal the formation of an alloy model (BTP-eC9:isoIDTIC) and a well-defined fibril-like network and enhanced crystallization of BHJ in the ternary blend. Slightly increased carrier mobilities, longer carrier lifetimes, and suppressed trap-assisted/bimolecular recombination are observed in the ternary BHJ-based devices compared to the binary PM6:BTP-eC9 BHJ cells. Moreover, because of the high surface energy (γ) and low glass-transition temperature (T_g) of BTP-eC9, the acceptor and donor tend to migrate toward the hole and electron collecting electrodes, respectively, during aging tests. Crucially, isoIDTIC with low γ and high T_g has a low diffusion coefficient and can suppress demixing in vertical stratification of the BHJ, resulting in an increase in T_{80} lifetime from 101 hours to 254 hours. Our results highlight the utilization of the nonfullerene acceptor with fibril-like morphology and high T_g as an important third component toward high-performance and stable ternary OPVs.

Received 27th October 2022,
Accepted 6th January 2023

DOI: 10.1039/d2ee03483b

rsc.li/ees

Broader context

Recently, several studies have been published in which fibril-like polymers are utilized as a third component to tune the morphology of a ternary blend, which is a simple approach to boost the overall cell performance of organic photovoltaic devices (OPVs). However, identification of this fibril-like network structure is hard to observe in nonfullerene and fullerene acceptors. To the best of our knowledge, there is no study focusing on the design or use of an acceptor that exhibits a fibril-like morphology as a third component in BHJs to optimize the morphology of ternary OPVs. Herein, we designed and synthesized a nonfullerene acceptor, isoIDTIC, that exhibits a fibril-like morphology as well as good compatibility and miscibility with the BTP-eC9 host acceptor in BHJ thin films. The resulting acceptor alloy (BTP-eC9:isoIDTIC) exhibits a well-defined fibrillar structure and an enhanced π–π stacking order when blended with the donor polymer PM6 to form the ternary PM6:BTP-eC9:isoIDTIC blend. The ensuing OPVs exhibit a PCE of 19%, which is attributed to slightly larger carrier mobilities, well-balanced hole and electron mobilities, longer carrier lifetimes, and reduced recombination in the ternary BHJ devices as compared to cells based on the binary PM6:BTP-eC9 blend. Importantly, apart from increasing the PCE, the lower surface energy and higher glass transition temperature of isoIDTIC than BTP-eC9 can effectively suppress the unfavourable vertical stratification of the donor and acceptor within the BHJ during aging tests. The resulting ternary PM6:BTP-eC9:isoIDTIC OPVs exhibit a longer T_{80} lifetime than PM6:BTP-eC9 cells (254 *vs.* 101 hours).

[a] *School of Physical Sciences, Great Bay University, Dongguan, 523000, China*
[b] *King Abdullah University of Science and Technology (KAUST), KAUST Solar Center (KSC), Thuwal 23955, Saudi Arabia*
[c] *Department of Chemistry, Korea University, Seoul 02841, Republic of Korea*
[d] *Department of Chemistry, University of Oxford, Oxford, OX1 3TA, UK. E-mail: yuanbao.lin@chem.ox.ac.uk*
[e] *Renewable and Sustainable Energy Institute, Department of Chemistry and Department of Chemical and Biological Engineering, University of Colorado Boulder, Boulder, CO 80303, USA*
[f] *Hoffmann Institute of Advanced Materials, Shenzhen Polytechnic, Shenzhen, Guangdong, 518000, China*

† Electronic supplementary information (ESI) available. See DOI: https://doi.org/10.1039/d2ee03483b

Introduction

Organic photovoltaic devices (OPVs) have attracted great research attention thanks to their potential advantages including low cost, light weight, mechanical flexibility, and large-scale manufacture.[1–5] Recently, the reported power conversion efficiencies (PCEs) of for this emerging renewable energy technology have reached 19% for single-junction OPVs due to the rapid development of photo-active organic material and device's

engineering,[6–10] approaching the predicted limit of PCE (~20%) for single-junction OPVs.[11]

Most of the reported high-efficiency single junction OPVs (*i.e.* those with PCEs over 18%) are based on the ternary bulk-heterojunction (BHJ) strategy[12] or tandem structure,[13] since simple binary blends lead to insufficient light absorption and/or unavoidable energy losses. However, fabricating tandem OPVs involves complex multilayer deposition, which limits their utilization. Hence, single-junction OPVs based on ternary BHJs, in which a guest donor or acceptor is incorporated into the host binary system, represent a simple approach to boost the overall cell performance.[14] For designing or selecting a desired third component for ternary blends, we typically select guest materials with complementary absorption to the absorption spectra of the components of the binary system, to enhance the light-harvesting ability, as well as to ensure the optimal highest occupied molecular orbital (HOMO) and lowest unoccupied molecular orbital (LUMO) energy levels, located between the host donor and acceptor, to form a cascade energy level alignment.[15–17] Moreover, as summarised in Table S1 (ESI†), most of the ternary OPVs with PCE > 18% rely on guest materials that simultaneously exhibit relatively good performance (PCE > 10%) when employed in guest binary blends.[6,8–10,12,18–24] Having this latter criterion as a requirement for the third component, however, could result in overlooking some promising candidates that could be useful as guest materials in high-performance OPVs.

Furthermore, recently, several studies have been published in which fibril-like polymers are utilized as a third component to tune the morphology of ternary blends.[12,20,21] Impressively, the D18 donor polymer with fibril-like morphology was employed as a guest material into the PM6:L8-BO blend, forming a refined double-fibril network morphology and achieving a PCE of 19.6% in ternary OPVs.[12] However, identification of this fibril-like network structure is hard to observe in nonfullerene and fullerene acceptors, as shown by atomic force microscopy (AFM) images of Y6, IDTIC, and $PC_{71}BM$ in Fig. S1 (ESI†). To the best of our knowledge, there is no study focusing on the design or use of an acceptor that exhibits a fibril-like morphology as a third component in the BHJ to optimize the morphology of ternary OPVs.

Herein, we designed and synthesized a nonfullerene acceptor, isoIDTIC, that exhibits a curved shape comprising four aliphatic chains arranged on the same side of the backbone, in contrast to the established IDTIC, which has symmetrically arranged chains on both sides. Although isoIDTIC has an absorption that overlaps with the PM6 donor, it exhibits a fibril-like morphology as well as good compatibility and miscibility with the BTP-eC9 host acceptor in BHJ thin films. The resulting acceptor alloy (BTP-eC9:isoIDTIC) exhibits a well-defined fibrillar structure and an enhanced π–π stacking order when blended with the donor polymer PM6 to form the ternary PM6:BTP-eC9:isoIDTIC blend. The ensuing OPVs exhibit a PCE of 19%, which is attributed to slightly larger carrier mobilities, well-balanced hole and electron mobilities, longer carrier lifetimes, and reduced recombination in the ternary BHJ devices as compared to cells based on the binary PM6:BTP-eC9 blend. Importantly, apart from increasing the PCE, the lower surface energy and higher glass transition temperature (T_g) of isoIDTIC than BTP-eC9, can effectively suppress the unfavourable vertical stratification of the donor and acceptor within the BHJ during aging tests. The resulting ternary PM6:BTP-eC9:isoIDTIC OPVs exhibit a longer T_{80} lifetime (the time required to reach 80% of the initial performance) than PM6:BTP-eC9 cells (254 *vs.* 101 hours).

Details of the synthesis of isoIDTIC are provided in Scheme 1, while the ^1H and ^{13}C NMR spectra of isoIDTIC are presented in Fig. S2 (ESI†). Negishi coupling of readily available diethyl 4,6-dibromoisophthalate (compound **1**) and thiophen-2-ylzinc(II) bromide afforded diester **2** in 87% yield, and **2** was then hydrolyzed to the diacid **3**. Intramolecular Friedel–Crafts acylation of compound **3** afforded the insoluble diketone **4**; this was followed by a Wolff–Kishner–Huang reduction to afford the alkylation precursor **5**. After alkylation of **5** under basic conditions with hexadecyl chains, the two thiophene rings were formylated to afford compound **7**, which was reacted with 2-(3-oxo-2,3-dihydro-1*H*-inden-1-ylidene)malononitrile to afford the final acceptor isoIDTIC. The short contact interaction between the sulfur of the thiophene ring and the oxygen atom of the carbonyl group, which is commonly seen in the IDIC and Y6 series, together with the bulky repulsion of the four linear chains, is anticipated to force the backbone to be curved into a "U" shape. 2D rotating frame overhauser enhancement spectroscopy (ROESY) as shown in Fig. S3 (ESI†) reveals a strong correlation between the thiophene proton (7.76 ppm) and the alkene proton (8.99 ppm), indicating that the two protons are close to each other spatially, and hence supporting the expected curved geometry.

Fig. 1a presents the molecular structures of the active materials used in this study, *i.e.* PM6 as the host donor, BTP-eC9 (C9) as the host acceptor, and isoIDTIC as the guest acceptor. The isoIDTIC acceptor shows good solubility in commonly used organic solvents such as chloroform, chlorobenzene, and *o*-dichlorobenzene. The UV-vis absorption spectra of PM6, BTP-eC9, and isoIDTIC neat films are shown in Fig. 1b. isoIDTIC exhibits an absorption from 300 to 660 nm, which is similar to that of the PM6 donor polymer. This overlapped absorption of donor and acceptor contributes to the limited light-harvesting ability in binary (PM6:isoIDTIC) devices. The optical bandgap estimated from the onsets of the absorption of the solid films is 1.90 eV for isoIDTIC, which is wider than those of PM6 (1.80 eV) and BTP-eC9 (1.57 eV). Moreover, the HOMO energy level of isoIDTIC, obtained from photoelectron spectroscopy in air (PESA) measurements (Fig. S4a and b, ESI†), is −5.88 eV, which is deeper than that of BTP-eC9 (−5.64 eV). The experimental HOMO/LUMO values are consistent with the density functional theory (DFT) calculations of the energies of the frontier orbitals of isoIDTIC and BTP-eC9. As shown in Fig. S4c and d and Table S2 (ESI†), the calculated HOMO/LUMO energy levels of isoIDTIC and BTP-eC9 are −5.83 eV/−3.28 eV and −5.65 eV/−3.63 eV, respectively. Hence, both theoretical calculations and experimental data suggest that isoIDTIC, as a guest acceptor, is unlikely to provide a cascade-like energy

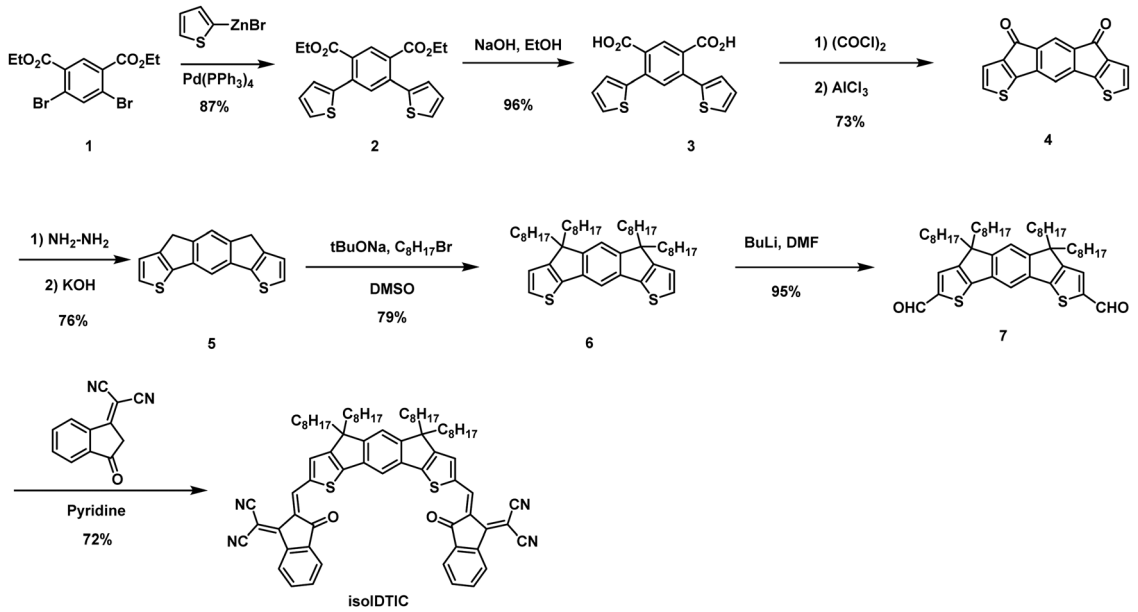

Scheme 1 Synthesis of isoIDTIC.

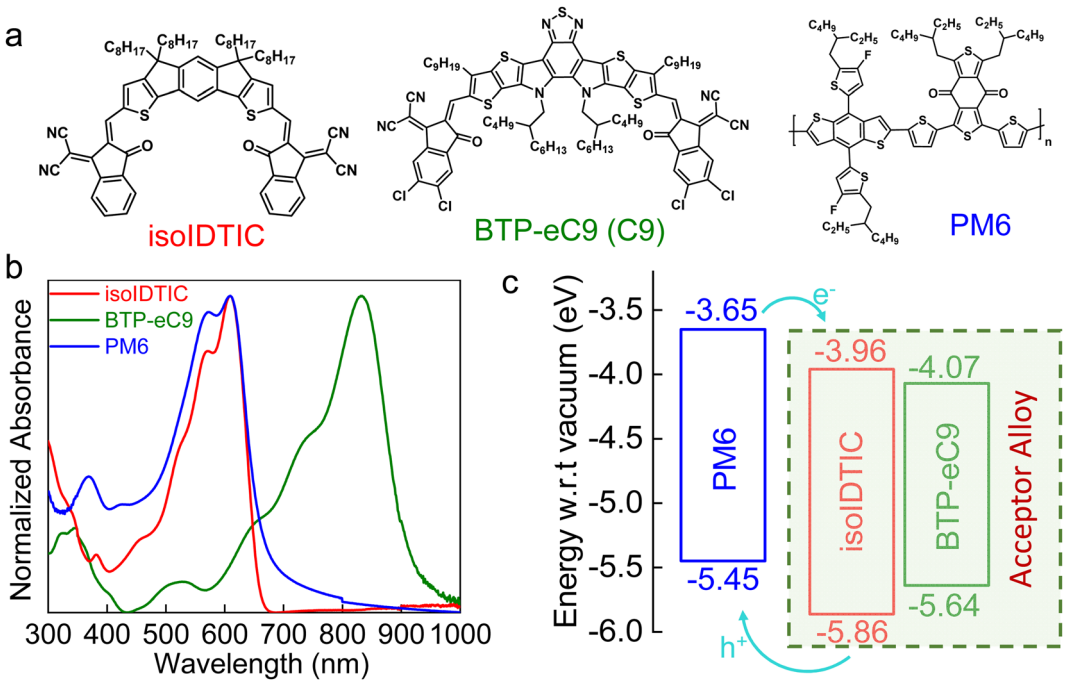

Fig. 1 (a) Chemical structures of isoIDTIC, BTP-eC9, and PM6. (b) Normalized UV-vis absorption spectra of PM6, BTP-eC9, and isoIDTIC solid films. (c) Energy diagrams of PM6, BTP-eC9, and isoIDTIC.

alignment when employed as a third component in a host PM6 and host BTP-eC9 ternary blend, as shown in Fig. 1c, as its HOMO energy level is too deep.

From a light harvesting and energy transfer perspective, isoIDTIC cannot be considered an ideal guest acceptor for a PM6:BTP-eC9 ternary blend.[25] However, there are several studies on efficient ternary BHJ systems based on alloy models, *i.e.* systems in which the third component (an acceptor or a donor) electronically couples with the host acceptor or donor due to excellent compatibility between the two donors or acceptors, and either an A1:A2 or a D1:D2 electronic alloy is formed.[16,18,24] To evaluate whether isoIDTIC forms an alloy with either the acceptor or donor, the contact angles and surface energies (γ) of the PM6, BTP-eC9, and isoIDTIC neat films were obtained and are given in Fig. S5 and Table S3 (ESI†). The values of γ of PM6, BTP-eC9, and isoIDTIC are 20.5, 25.6, and 29.4 mN m^{-1},

respectively. Based on the surface energy results, the Flory–Huggins interaction parameter χ can be estimated using the equation: $\chi_{A:B} \propto \left(\sqrt{\gamma_A} - \sqrt{\gamma_B}\right)^2$, where γ_A and γ_B are the surface energy values of components A and B.[26] The χ parameter was calculated to be 0.84, 0.30, and 0.13 for PM6:BTP-eC9, PM6:isoIDTIC, and BTP-eC9:isoIDTIC blends, respectively. The χ value for BTP-eC9:isoIDTIC is the lowest of the three binary blends, indicating that the nonfullerene acceptor isoIDTIC is compatible with the host acceptor BTP-eC9. This compatibility between BTP-eC9 and isoIDTIC can be further investigated using the interfacial tension (γ_{AB}) calculated according to Neumann's equation:[27] $\gamma_{AB} = \gamma_A + \gamma_B - 2(\gamma_A\gamma_B)^{0.5}e^{\left[-\beta(\gamma_A-\gamma_B)^2\right]}$, where β = 1.15 × 10^{-4} m^4 mJ^{-2}. As summarized in Table S4 (ESI†), the interfacial tension between BTP-eC9 and isoIDTIC is 0.22 mN m^{-1}, which is lower than the interfacial tension of PM6:BTP-eC9 (1.30 mN m^{-1}) and PM6:isoIDTIC (0.45 mN m^{-1}). Both Flory–Huggins interaction and interfacial tension results support the idea that the isoIDTIC acceptor has good miscibility and compatibility with the BTP-eC9 acceptor and can form a BTP-eC9:isoIDTIC acceptor alloy within the PM6:BTP-eC9:isoIDTIC ternary blend.

AFM measurements were used to explore the surface topography of blend films. All of them were spin-coated on glass substrates and then annealed at 100 °C for 10 minutes. As shown in Fig. 2a and b, there are some obvious sunken surfaces (~2 μm^2) with a height of ~40 nm on the BTP-eC9 film, while some nodular BTP-eC9 domains are observed from the high-resolution AFM (Fig. 2c and d), suggesting that the BTP-eC9 molecules with a fairly low T_g of 174 °C (Fig. S6, ESI†) easily aggregate during annealing according to the previous reports.[28,29] In contrast, isoIDTIC forms a smooth surface (Fig. 2e and f) with a much lower root-mean-square (RMS) surface roughness value as compared to the BTP-eC9 film (4.9 *vs.* 11.7 nm). Interestingly, unlike other conventional nonfullerene acceptors including Y6, IDTIC, and BTP-eC9 having nodular surface morphologies (Fig. S1, ESI† and Fig. 2d), a clearly fibril-like network is observed in the isoIDTIC film from high-resolution AFM (Fig. 2g and h), indicating that isoIDTIC with fibril-like morphology will possibly improve the morphology in the ternary blend. Moreover, it should be pointed out that the annealing treatment is one of the key factors to form the fibril-like network of the isoIDTIC film since the clearly fibril-like network is absent in the unannealed isoIDTIC film (Fig. S7, ESI†). In contrast, the annealing treatment has a negligible impact on the BTP-eC9 film because BTP-eC9 (both without and with annealing) exhibits a nodular surface. However, a dedicated study of the original reasons and design rules for the fibril-like network in a small molecule would be required and should be the subject of a future investigation.

Hence, we characterized the morphology of the BHJ (PM6:BTP-eC9) in the absence and presence of isoIDTIC (Fig. 3). Although BTP-eC9 aggregates easily and has a nodular morphology, the PM6:BTP-eC9 blends still have a fibrillar network arising from the PM6 polymer with a fibril-like morphology (Fig. S8, ESI†). Interestingly, when incorporating isoIDTIC, the ternary film (PM6:BTP-eC9:isoIDTIC) becomes smoother with a slightly smaller RMS roughness, and the fibril texture becomes more distinct and well-defined in both height images and cross-section profiles than in the binary blend, which may benefit charge transport in devices.[30,31] Besides forming a distinct and well-defined fibrillar network, the isoIDTIC third component also enhances the crystallinity of the ternary BHJ layer, as shown by the grazing-incidence wide-angle X-ray

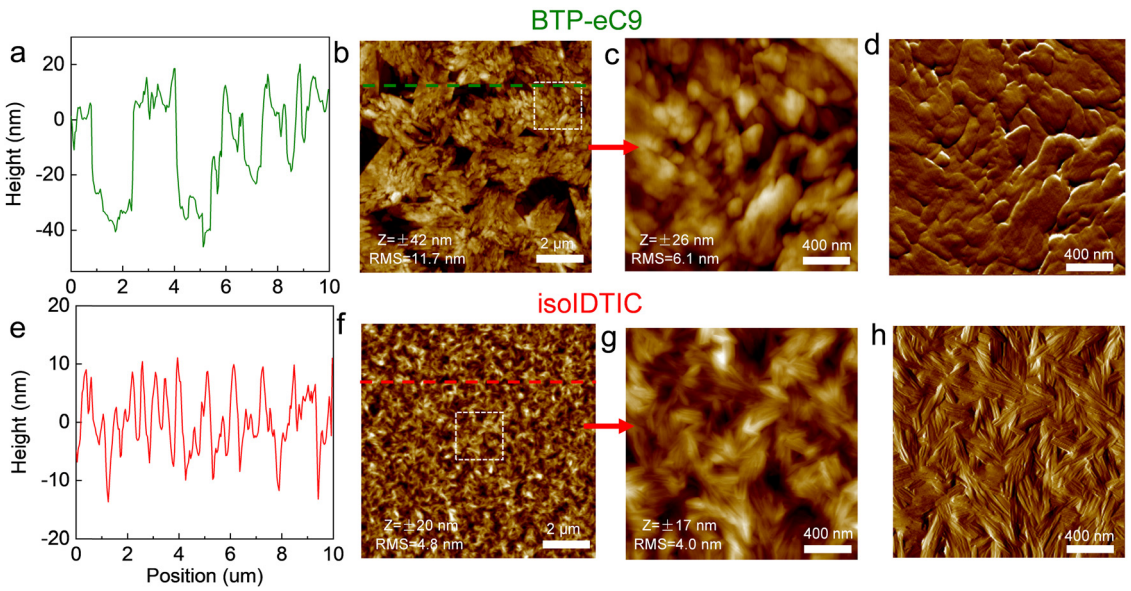

Fig. 2 (a) The height profile corresponding to the dashed line in (b). (b) AFM topography of the BTP-eC9 solid film. (c and d) High-resolution AFM height and phase images corresponding to the dashed frame in (b). (e–h) The corresponding height profile and AFM images of the isoIDTIC solid film.

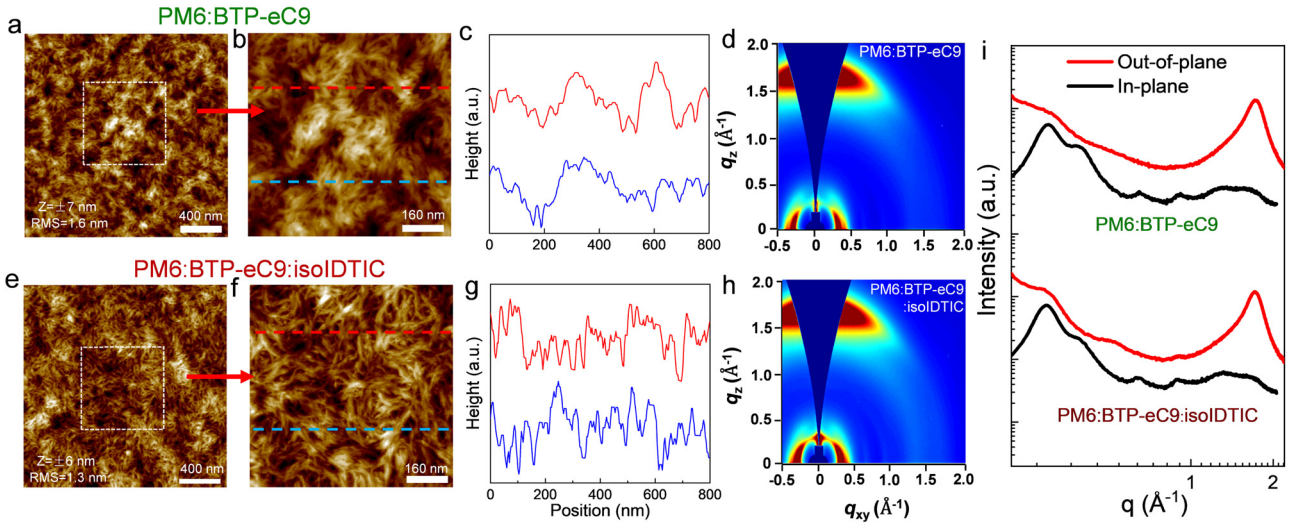

Fig. 3 (a) AFM topography of the binary PM6:BTP-eC9 blend. (b) High-resolution AFM height image corresponding to the dashed frame in (a). (c) Height profile of the image in (b). (d) GIWAXS patterns for the PM6:BTP-eC9 blend film. (e–h) The corresponding AFM images, height profile, and GIWAXS patterns of the ternary PM6:BTP-eC9:isoIDTIC blend film. (i) Scattering profiles of in-plane and out-of-plane for PM6:BTP-eC9 and PM6:BTP-eC9:isoIDTIC blend films.

scattering (GIWAXS) measurements (Fig. 3). Both the binary (PM6:BTP-eC9) and ternary (PM6:BTP-eC9:isoIDTIC) films exhibit strong face-on dominant mixed orientation with a π–π stacking (010) peak at q_z = 1.71 Å^{-1} along the out-of-plane (OOP) direction, while the ternary film shows a similar lamellar stacking (100) peak at q_z ∼ 0.30 Å^{-1} corresponding to the repeat distance along the in-plane (IP) direction. Moreover, based on the OOP (010) and IP (100) peaks (Table S5, ESI†), the crystal coherence length (CCL) values of the BHJ increased somewhat (13% from 21.10 Å to 23.86 Å, and 15% from 74.40 Å to 85.68 Å) with the addition of the isoIDTIC third component, thus leading to the enhancement in crystallization in both π–π stacking and lamellar stacking, and further assisting charge transport and improving the device performance.[10]

According to the above observations, the isoIDTIC guest acceptor could form an electronic alloy with BTP-eC9 as well as optimize the morphology of the BHJ in the ternary blend. To demonstrate that these features could enhance the photovoltaic properties, the OPV cells with the standard architecture based on ITO/Cl-2PACz/BHJ/PNDIT-F3N/Ag (Fig. 4a) were investigated, where the Cl-2PACz self-assembled monolayer (SAM) is a hole-selective contact on ITO.[32] The current density–voltage

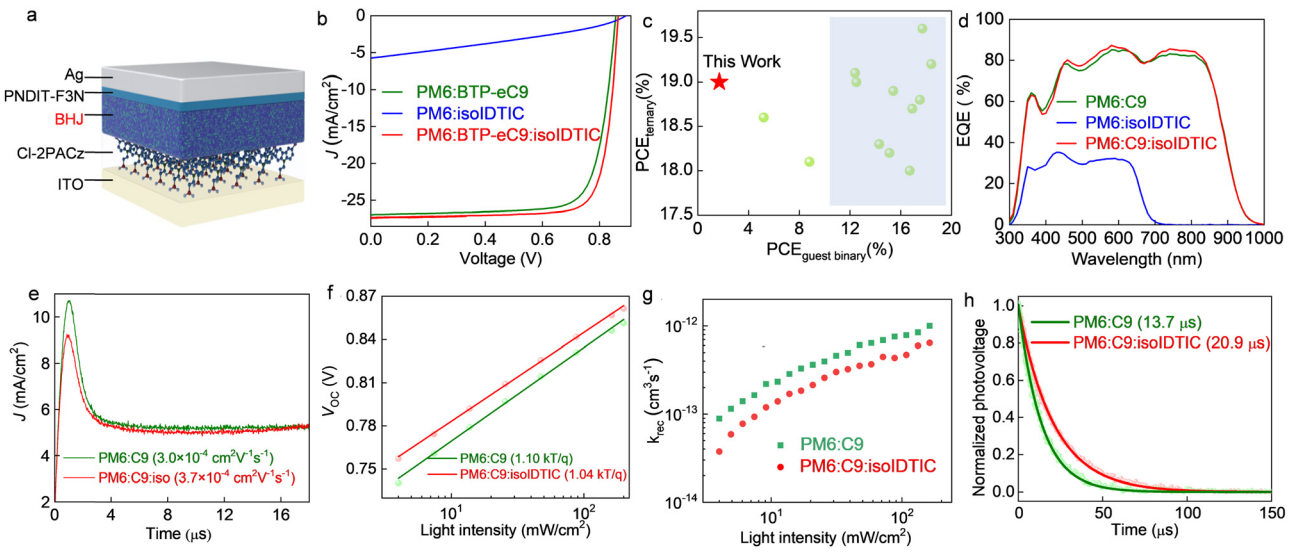

Fig. 4 (a) Schematic architecture of an OPV. (b) *J*–*V* curves for the optimized devices based on PM6:BTP-eC9, PM6:isoIDTIC, and PM6:BTP-eC9:isoIDTIC. (c) Summary of the ternary BHJ studies; the *X*-axis represents the PCEs of the guest binary systems. (d) The EQE curves correspond to devices in (b). (e) photo-CELIV, (f) light intensity dependence of the V_{OC}, (g) bimolecular recombination rate constant (k_{rec}), and (h) TPV spectra for the optimized binary (PM6:BTP-eC9) and ternary (PM6:BTP-eC9:isoIDTIC) OPVs.

(*J*–*V*) curves of the ternary BHJ cells with various isoIDTIC contents are presented in Fig. S9a and the details are provided in Table S6 (ESI†), while representative *J*–*V* curves are displayed in Fig. 4b and the details are provided in Table 1. Moreover, as summarised in Fig. S9b (ESI†), the open circuit voltage (V_{OC}) of OPV cells is shown to be linearly correlated with the ratios of the third component. The improved V_{OC} in ternary devices compared with the binary blend is attributed to the formation of alloy-like composites between BTP-eC9 and isoIDTIC, leading to the changed electronic properties of BTP-eC9:isoIDTIC.[24,33] As shown in Fig. S10 and Table S7 (ESI†), the BTP-eC9:isoIDTIC alloy has LUMO and HOMO levels of 3.96 eV and 5.61 eV, which are between those of BTP-eC9 and isoIDTIC and in agreement with the previous ternary BHJ based on an alloy model.[34,35]

Moreover, the binary PM6:BTP-eC9-based OPVs yield a PCE of 17.9%, with a V_{OC} of 0.857 V, a short-circuit current (J_{SC}) of 26.95 mA cm^{-2}, and a fill factor (FF) of 77.5%. In contrast, the OPVs with the binary PM6:isoIDTIC blend exhibit enhanced V_{OC} (0.893 V) due to the higher LUMO of isoIDTIC but with significantly reduced J_{SC} (5.75 mA cm^{-2}) and FF (32.3%), eventually along with a very low PCE of 1.7%. With 10 wt% isoIDTIC, the ternary OPVs exhibit superior performance with an enhanced PCE (19.0%) owing to the simultaneously increased V_{OC} (0.866 V), J_{SC} (27.30 mA cm^{-2}), and FF (80.4%), and a low series resistance (R_S) of 1.45 Ω cm^2. As summarised in Table S1 (ESI†) and Fig. 4c, most ternary blends reported in the literature utilized high-performance guest materials (PCEs > 10% in binaries). In contrast, here we realized ternary OPVs with a maximum PCE of 19% by incorporating a third component that performs poorly in binary cells (PCE < 2%).

To elucidate the origin of the variation in J_{SC} seen in the different cells, we measured the external quantum efficiency (EQE) spectra of all devices (Fig. 4d). The integrated photocurrent density (J_{cal}) deduced from the EQE matches the J_{SC} from *J*–*V* curves within ±2.5% (Table 1). The EQE response of PM6:isoIDTIC-based devices is from 330 to 680 nm with an average value of around 28%, resulting in a low photocurrent (J_{cal}: 5.66 mA cm^{-2}). Moreover, OPVs based on the PM6:BTP-eC9:isoIDTIC ternary blends exhibit a slightly increased photoresponse at wavelengths of around 450–620 nm and 700–830 nm, which is in agreement with the absorption coefficient results (Fig. S11, ESI†), contributing to a higher J_{SC} in the ternary device.

Table 1 Photovoltaic parameters of binary and ternary OPVs, measured under AM 1.5 G illumination at 100 mW cm^{-2}

BHJ	V_{OC} [V]	J_{SC} [mA cm^{-2}]	J_{cal}[a] [mA cm^{-2}]	FF [%]	PCE[b] [%]	R_s [Ω cm^2]
PM6:C9	0.857	26.95	26.29	77.5	17.9 (17.7 ± 0.3)	2.15
PM6:isoIDTIC	0.893	5.75	5.66	32.3	1.7 (1.5 ± 0.2)	46.3
PM6:C9:isoIDTIC	0.866	27.30	26.64	80.4	19.0 (18.7 ± 0.3)	1.45

[a] Calculated J_{SC} from EQE measurements. [b] The values in parentheses are average PCE values obtained from 20 different cells.

Next, we performed electrochemical impedance spectroscopy (EIS) measurements to assess the electrical properties of OPVs, especially the BHJ resistance (R_{bhj}).[36,37] Fig. S12 (ESI†) shows the Nyquist plots measured from OPV cells, and the fitted results are summarised in Table S8 (ESI†). The R_{bhj} in the ternary BHJ (PM6:BTP-eC9:isoIDTIC) device is lower than that of the binary PM6:BTP-eC9 based device (85.1 Ω *vs.* 105.2 Ω), which is attributed to the well-defined fibril structure and the improved crystallization of the PM6:BTP-eC9:isoIDTIC blend (Fig. 3), which results in improved charge transport. The charge transport across these blends was studied *via* the space-charge limited current (SCLC) analysis using hole-only and electron-only devices to probe this effect.[38] Fig. S13 and Table S9 (ESI†) show the calculated hole (μ_h) and electron (μ_e) mobilities. Evidently, the μ_h values remain similar (5.66×10^{-4} *vs.* 6.10×10^{-4} cm^2 V^{-1} s^{-1}) before and after isoIDTIC addition, while the μ_e increased by 40% from 3.35×10^{-4} to 4.74×10^{-4} cm^2 V^{-1} s^{-1}. The enhanced charge transport is also observed *via* photo-induced charge-carrier extraction from linearly increasing voltage (photo-CELIV)[39] measurements (Fig. 4e). The mobility (μ) of the charge carriers in OPVs with PM6:BTP-eC9:isoIDTIC is 3.7×10^{-4} cm^2 V^{-1} s^{-1}, which is slightly higher than that in PM6:BTP-eC9 cells (3.0×10^{-4} cm^2 V^{-1} s^{-1}). We attribute this increase to the formation of the well-defined fibrillar structure in ternary blends.[31] Apart from the faster charge transport, isoIDTIC also contributes to a well-balanced μ_h/μ_e ratio (1.69 to 1.29) by further enhancing the μ_e, resulting in both enhanced FF and J_{SC} of OPVs by balancing hole and electron transport and facilitating better charge collection.[40] Fig. 4f shows the dependence of V_{OC} on the incident light intensity, in which the slope is taken as nkT/q, where n is the constant, k is the Boltzmann constant, T is the temperature, and q is the elementary charge.[41] OPVs made with the ternary PM6:BTP-eC9:isoIDTIC yield a slope of 1.04 kT/q, which is slightly lower than that of the binary system (1.10 kT/q), suggesting the slightly reduced trap-assisted recombination in ternary cells.

Further insights into charge recombination across the device with and without isoIDTIC were obtained by studying the bimolecular recombination rate constants (k_{rec}) as a function of light intensity (Fig. S14, ESI†). Here, $k_{rec} = 1/(\lambda + 1)n\tau$, where λ is the recombination order, n is the carrier density, and τ is the carrier lifetime.[42,43] As shown in Fig. 4g, k_{rec} for the ternary device is lower than that calculated for the binary PM6:BPT-eC9 cell. Moreover, from transient photovoltage (TPV) measurements in Fig. 4h, the devices with isoIDTIC exhibit a longer carrier lifetime than those without it (20.9 μs *vs.* 13.7 μs). The suppressed bimolecular recombination and longer carrier lifetime in the ternary BHJ OPV are attributed to the well-defined fibrillar structure as well as enhanced π–π stacking observed in the ternary blends.[44,45]

Besides the improved PCE, the stability of OPVs under illumination is simultaneously important for any commercialization of OPVs.[46] As shown in Fig. 5a, the T_{80} lifetime of the ternary OPV is 254 hours, which is longer than the T_{80} (101 hours) for PM6:BTP-eC9 devices. To further understand

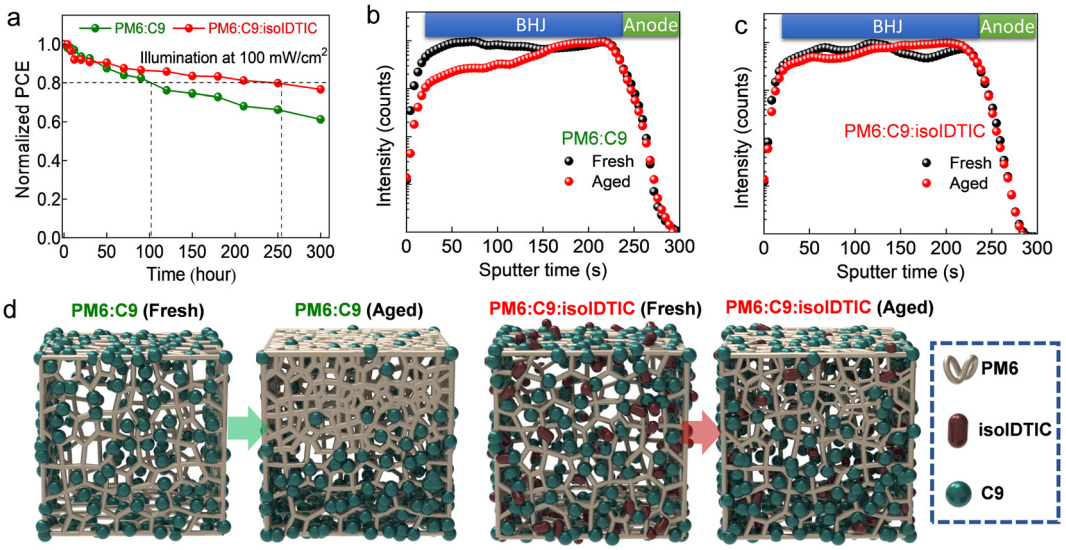

Fig. 5 (a) Evolution of normalized PCEs of OPVs based on PM6:BTP-eC9 and PM6:BTP-eC9:isoIDTIC. (b and c) The normalized ToF-SIMS intensity of Cl^- against the sputtering time. (d) The schematic diagram of the vertical distribution of donors and acceptors in fresh and aged BHJ films.

the enhanced stability of the devices with isoIDTIC, time-of-flight secondary ion mass spectrometry (ToF-SIMS) is employed to detect the vertical stratification of the BTP-eC9 component in the BHJ by tracking the Cl^- signal (Cl is found in BTP-eC9 but not in the PM6 or isoIDTIC). It should be pointed out that the Cl-2PACz SAM also contains Cl atoms and this may affect the apparent distribution signal of BTP-eC9. So, Br-2PACz SAM, which has a similar surface energy and energy levels to Cl-2PACz (Fig. S15, ESI†),[32] was used as the hole-extracting interlayer on ITO for the sole purpose of ToF-SIMS measurements. In the fresh PM6:BTP-eC9 devices, the Cl^- intensity is uniform under various sputter times (Fig. 5b), suggesting that the BTP-eC9 molecules are homogeneously distributed vertically within the BHJ. In contrast, the Cl^- intensity in the vicinity of the hole-collecting side (ITO/SAM) is higher than that in the top and middle of the BHJ for the aged device, indicating that BTP-eC9 has preferentially migrated towards the bottom of the BHJ and aggerated at the SAM surface during the stability test. Moreover, the F^- signal, representing PM6 in the aged PM6:BTP-eC9 binary blend cells (Fig. S14a, ESI†), weakens gradually with the increasing sputtering time relative to that of the fresh sample, meaning that more of the PM6 is accumulated at the top surface of the BHJ.

Interestingly, in the aged ternary PM6:BTP-eC9:isoIDTIC devices (Fig. 5c), although the Cl^- intensities also increase with the increasing sputter time, a smaller gradient and higher Cl^- concentration close to the top surface are observed relative to what is seen in the aged binary PM6:BTP-eC9 case. Similarly, the F^- intensities in the aged ternary BHJ (Fig. S16b, ESI†) are also slightly reduced close to the BHJ bottom, but they are still higher than those in the aged binary BHJ. The above results indicated that the migration of BTP-eC9 and PM6 to give an unfavorable vertical stratification of the donor and acceptor during aging is somewhat suppressed in the BHJ with isoIDTIC, which contributes to the improved stability of the PM6:BPT-eC9:isoIDTIC based OPVs (Fig. 5a). This unfavorable vertical stratification in the aged binary system results in large phase separation and aggregation as compared to a fresh binary BHJ film according to AFM measurements (Fig. S17, ESI†), while this spinodal decomposition is suppressed in the aged ternary BHJ with the isoIDTIC third component as shown in Fig. 5d.

The different vertical stratification of BHJ before and after adding isoIDTIC can be explained by the higher surface energies (γ) of BTP-eC9 as compared to PM6 (29.4 mN m^{-1} *vs.* 20.3 mN m^{-1}). Hence, the BTP-eC9 molecules preferentially migrate towards the higher γ interface of the ITO/SAM hole-collecting electrode (40 mN m^{-1}) during aging.[47,48] However, the lower γ of isoIDTIC as compared to BTP-eC9 (25.6 mN m^{-1} *vs.* 29.4 mN m^{-1}), and its good miscibility with BTP-eC9 (Tables S3 and S4, ESI†), results in the BTP-eC9:isoIDTIC alloy that exhibits a reduced γ value from 29.4 to 26.5 mN m^{-1}. Hence, though both the aged binary and ternary systems exhibit unfavourable vertical stratification, the ternary BHJ showed a smaller gradient. Moreover, the high Flory–Huggins interaction parameter $\chi_{PM6:BTP-eC9}$ indicates the instability of the association of the two immiscible components between PM6 and BTP-eC9, resulting in spinodal decomposition and unfavorable vertical stratification observed in the aged PM6:BTP-eC9 binary BHJ, which is in agreement with the previous reports.[49–51] However, the addition of compatible isoIDTIC in PM6:BTP-eC9 contributes to a decreased Flory–Huggins interaction parameter, resulting in the suppressed unfavorable vertical stratification. Apart from the effect of surface energy and compatibility on the energetic driving force for vertical stratification, the T_g values of the individual acceptors might also affect the kinetics of stratification. As presented in Fig. S6 (ESI†), the T_g values of BTP-eC9 and isoIDTIC are obtained from differential scanning calorimetry (DSC), showing that isoIDTIC has a higher T_g as compared to the BTP-eCP (206 °C

*vs.*174 °C). Since nonfullerene acceptors with a higher T_g are known to exhibit a lower diffusion coefficient and, as such, suppressed stratification within the BHJ,[28,29,52] the addition of isoIDTIC could contribute to the improved operational stability observed. This important observation could lead to new design rules for the development of high-performance OPVs.

In summary, a new nonfullerene acceptor, isoIDTIC, was designed, synthesized and applied as the third component in high-efficiency ternary organic solar cells. Owing to its good miscibility with BTP-eC9, the addition of isoIDTIC resulted in an acceptor alloy phase characterized by a fibrillar microstructure when incorporated into the ternary PM6:BTP-eC9:isoIDTIC blend. OPV cells based on the PM6:BTP-eC9:isoIDTIC blend exhibited an enhanced PCE of 19.0%. To the best of our knowledge, this is the first study focusing on designing an acceptor with fibril-like morphology for ternary BHJ OPVs. Moreover, we find that the lower surface energy and higher glass transition temperature of isoIDTIC efficiently suppress the migration of BTP-eC9 molecules towards the ITO/SAM electrode during the aging test, resulting in OPV cells with a longer operational lifetime. The present work provides valuable guidelines for the design of acceptor molecules with fibril-like morphology specifically for boosting both the PCE and operational stability of multi-component OPVs.

Author contributions

Y. L. and H. C. conceived the idea. H. C. synthesized the photovoltaic materials. Y. Z., S. B., and S. R. M. synthesized the self-assembled monolayer materials. Y. L. prepared, optimized, and characterized the photovoltaic devices. S. Y. J. and H. Y. W. characterized the GIWAXS. J. T. contributed to the DFT calculations and ROESY measurements. M. A. and S. G. characterized the materials. H. H. characterized SIMS. D. R. N. characterized AFM. Y. L., I. M., H. C., and T. D. A. prepared the manuscript. All authors contributed to editing the manuscript. Y. L. supervised and directed the project.

Conflicts of interest

The authors declare no conflict of interest.

Acknowledgements

This research was funded in part, by the European Union's Horizon 2020 research and innovation programme under grant agreement no. 952911, project BOOSTER, grant agreement no. 862474, project RoLA-FLEX, and grant agreement no. 101007084 CITYSOLAR, as well as the EPSRC Project EP/T026219/1 EP/W017091/1. T. D. A. and Y. L. acknowledge the King Abdullah University of Science and Technology (KAUST) Office of Sponsored Research (OSR) under Awards No. OSR-2018-CARF/CCF-3079 and OSR-2019-CRG8-4095. H. C. was supported by the open research fund of Songshan Lake Materials Laboratory 2022SLABFN06. Y. Z., S. B., and S. R. M. acknowledge funding from the Department of the Navy, Office of Naval Research as part of a Multidisciplinary University Research Initiative, Award No., N00014-21-1-2180. H. Y. W. acknowledges the financial support from the National Research Foundation (NRF) of Korea (2019R1A6A1A11044070).

References

1 Y. Jiang, X. Dong, L. Sun, T. Liu, F. Qin, C. Xie, P. Jiang, L. Hu, X. Lu, X. Zhou, W. Meng, N. Li, C. J. Brabec and Y. Zhou, *Nat. Energy*, 2022, **7**, 352–359.
2 Y. Lin, B. Adilbekova, Y. Firdaus, E. Yengel, H. Faber, M. Sajjad, X. Zheng, E. Yarali, A. Seitkhan and O. M. Bakr, *Adv. Mater.*, 2019, **31**, 1902965.
3 Y. Li, X. Huang, K. Ding, H. K. M. Sheriff, Jr., L. Ye, H. Liu, C. Z. Li, H. Ade and S. R. Forrest, *Nat. Commun.*, 2021, **12**, 5419.
4 J. Wang, P. Xue, Y. Jiang, Y. Huo and X. Zhan, *Nat. Rev. Chem.*, 2022, **6**, 614–634.
5 G. Zhang, F. R. Lin, F. Qi, T. Heumuller, A. Distler, H. J. Egelhaaf, N. Li, P. C. Y. Chow, C. J. Brabec, A. K. Jen and H. L. Yip, *Chem. Rev.*, 2022, **122**, 14180.
6 R. Sun, Y. Wu, X. Yang, Y. Gao, Z. Chen, K. Li, J. Qiao, T. Wang, J. Guo, C. Liu, X. Hao, H. Zhu and J. Min, *Adv. Mater.*, 2022, 2110147.
7 P. Bi, S. Zhang, Z. Chen, Y. Xu, Y. Cui, T. Zhang, J. Ren, J. Qin, L. Hong, X. Hao and J. Hou, *Joule*, 2021, **5**, 2408–2419.
8 Y. Cui, Y. Xu, H. Yao, P. Bi, L. Hong, J. Zhang, Y. Zu, T. Zhang, J. Qin, J. Ren, Z. Chen, C. He, X. Hao, Z. Wei and J. Hou, *Adv. Mater.*, 2021, **33**, 2102420.
9 L. Zhan, S. Li, Y. Li, R. Sun, J. Min, Z. Bi, W. Ma, Z. Chen, G. Zhou, H. Zhu, M. Shi, L. Zuo and H. Chen, *Joule*, 2022, **6**, 662–675.
10 K. Chong, X. Xu, H. Meng, J. Xue, L. Yu, W. Ma and Q. Peng, *Adv. Mater.*, 2022, **34**, 2109516.
11 Y. Firdaus, V. M. Le Corre, J. I. Khan, Z. Kan, F. Laquai, P. M. Beaujuge and T. D. Anthopoulos, *Adv. Sci.*, 2019, **6**, 1802028.
12 L. Zhu, M. Zhang, J. Xu, C. Li, J. Yan, G. Zhou, W. Zhong, T. Hao, J. Song, X. Xue, Z. Zhou, R. Zeng, H. Zhu, C.-C. Chen, R. C. I. MacKenzie, Y. Zou, J. Nelson, Y. Zhang, Y. Sun and F. Liu, *Nat. Mater.*, 2022, **21**, 656.
13 Z. Zheng, J. Wang, P. Bi, J. Ren, Y. Wang, Y. Yang, X. Liu, S. Zhang and J. Hou, *Joule*, 2022, **6**, 171–184.
14 N. Gasparini, A. Salleo, I. McCulloch and D. Baran, *Nat. Rev. Mater.*, 2019, **4**, 229.
15 N. Y. Doumon, L. Yang and F. Rosei, *Nano Energy*, 2022, **94**, 106915.
16 X. Xu, Y. Li and Q. Peng, *Adv. Mater.*, 2022, 2107476.
17 Y. Li, Y. Cai, Y. Xie, J. Song, H. Wu, Z. Tang, J. Zhang, F. Huang and Y. Sun, *Energy Environ. Sci.*, 2021, **14**, 5009.
18 P. Bi, S. Zhang, Z. Chen, Y. Xu, Y. Cui, T. Zhang, J. Ren, J. Qin, L. Hong, X. Hao and J. Hou, *Joule*, 2021, **5**, 2408.
19 Y. Cai, Y. Li, R. Wang, H. Wu, Z. Chen, J. Zhang, Z. Ma, X. Hao, Y. Zhao, C. Zhang, F. Huang and Y. Sun, *Adv. Mater.*, 2021, **33**, 2101733.

20 T. Zhang, C. An, P. Bi, Q. Lv, J. Qin, L. Hong, Y. Cui, S. Zhang and J. Hou, *Adv. Energy Mater.*, 2021, **11**, 2101705.
21 W. Peng, Y. Lin, S. Y. Jeong, Z. Genene, A. Magomedov, H. Y. Woo, C. Chen, W. Wahyudi, Q. Tao, J. Deng, Y. Han, V. Getautis, W. Zhu, T. D. Anthopoulos and E. Wang, *Nano Energy*, 2022, **92**, 106681.
22 L. Zhan, S. Li, X. Xia, Y. Li, X. Lu, L. Zuo, M. Shi and H. Chen, *Adv. Mater.*, 2021, **33**, 2007231.
23 Y. Zeng, D. Li, H. Wu, Z. Chen, S. Leng, T. Hao, S. Xiong, Q. Xue, Z. Ma, H. Zhu and Q. Bao, *Adv. Funct. Mater.*, 2021, **32**, 2110743.
24 F. Liu, L. Zhou, W. Liu, Z. Zhou, Q. Yue, W. Zheng, R. Sun, W. Liu, S. Xu, H. Fan, L. Feng, Y. Yi, W. Zhang and X. Zhu, *Adv. Mater.*, 2021, **33**, 2100830.
25 T. Ameri, P. Khoram, J. Min and C. J. Brabec, *Adv. Mater.*, 2013, **25**, 4245–4266.
26 A. Maiti and S. McGrother, *J. Chem. Phys.*, 2004, **120**, 1594–1601.
27 D. Li and A. W. Neumann, *J. Colloid Interface Sci.*, 1990, **137**, 304–307.
28 Y. Qin, N. Balar, Z. Peng, A. Gadisa, I. Angunawela, A. Bagui, S. Kashani, J. Hou and H. Ade, *Joule*, 2021, **5**, 2129–2147.
29 M. Ghasemi, H. Hu, Z. Peng, J. J. Rech, I. Angunawela, J. H. Carpenter, S. J. Stuard, A. Wadsworth, I. McCulloch, W. You and H. Ade, *Joule*, 2019, **3**, 1328–1348.
30 T. Liu, L. Huo, S. Chandrabose, K. Chen, G. Han, F. Qi, X. Meng, D. Xie, W. Ma and Y. Yi, *Adv. Mater.*, 2018, **30**, 1707353.
31 Y. Xie, Y. Cai, L. Zhu, R. Xia, L. Ye, X. Feng, H. L. Yip, F. Liu, G. Lu, S. Tan and Y. Sun, *Adv. Funct. Mater.*, 2020, **30**, 2002181.
32 Y. Lin, Y. Zhang, J. Zhang, M. Marcinskas, T. Malinauskas, A. Magomedov, M. I. Nugraha, D. Kaltsas, D. R. Naphade, G. T. Harrison, A. El-Labban, S. Barlow, S. De Wolf, E. Wang, I. McCulloch, L. Tsetseris, V. Getautis, S. R. Marder and T. D. Anthopoulos, *Adv. Energy Mater.*, 2022, **12**, 2202503.
33 D. Wang, R. Qin, G. Zhou, X. Li, R. Xia, Y. Li, L. Zhan, H. Zhu, X. Lu, H.-L. Yip, H. Chen and C.-Z. Li, *Adv. Mater.*, 2020, **32**, 2001621.
34 L. Zhan, S. Li, T.-K. Lau, Y. Cui, X. Lu, M. Shi, C.-Z. Li, H. Li, J. Hou and H. Chen, *Energy Environ. Sci.*, 2020, **13**, 635–645.
35 X. Huang, X. Liu, K. Ding and S. R. Forrest, *Mater. Horiz.*, 2020, **7**, 244–251.
36 E. P. Yao, C. C. Chen, J. Gao, Y. S. Liu, Q. Chen, M. Cai, W. C. Hsu, Z. R. Hong, G. Li and Y. Yang, *Sol. Energy Mater. Sol. Cells*, 2014, **130**, 20–26.
37 Y. Lin, C. Cai, Y. Zhang, W. Zheng, J. Yang, E. Wang and L. Hou, *J. Mater. Chem. A*, 2017, **5**, 4093–4102.
38 V. Mihailetchi, J. Wildeman and P. Blom, *Phys. Rev. Lett.*, 2005, **94**, 126602.
39 T. M. Clarke, C. Lungenschmied, J. Peet, N. Drolet and A. J. Mozer, *Adv. Energy Mater.*, 2015, **5**, 1401345.
40 D. Bartesaghi, C. Perez Idel, J. Kniepert, S. Roland, M. Turbiez, D. Neher and L. J. Koster, *Nat. Commun.*, 2015, **6**, 7083.
41 A. K. Kyaw, D. H. Wang, V. Gupta, W. L. Leong, L. Ke, G. C. Bazan and A. J. Heeger, *ACS Nano*, 2013, **7**, 4569–4577.
42 B. C. O'Regan, K. Bakker, J. Kroeze, H. Smit, P. Sommeling and J. R. Durrant, *J. Phys. Chem. B*, 2006, **110**, 17155–17160.
43 R.-Z. Liang, M. Babics, V. Savikhin, W. Zhang, V. M. Le Corre, S. Lopatin, Z. Kan, Y. Firdaus, S. Liu, I. McCulloch, M. F. Toney and P. M. Beaujuge, *Adv. Energy Mater.*, 2018, **8**, 1800264.
44 Z. Li and C. R. McNeill, *J. Appl. Phys.*, 2011, **109**, 074513.
45 A. Pockett, H. K. H. Lee, B. L. Coles, W. C. Tsoi and M. J. Carnie, *Nanoscale*, 2019, **11**, 10872–10883.
46 X. Xu, J. Xiao, G. Zhang, L. Wei, X. Jiao, H.-L. Yip and Y. Cao, *Sci. Bull.*, 2020, **65**, 208–216.
47 L. Huang, G. Wang, W. Zhou, B. Fu, X. Cheng, L. Zhang, Z. Yuan, S. Xiong, L. Zhang, Y. Xie, A. Zhang, Y. Zhang, W. Ma, W. Li, Y. Zhou, E. Reichmanis and Y. Chen, *ACS Nano*, 2018, **12**, 4440–4452.
48 H. Zhang, Y. Li, X. Zhang, Y. Zhang and H. Zhou, *Mater. Chem. Front.*, 2020, **4**, 2863–2880.
49 M. Kim, J. Lee, S. B. Jo, D. H. Sin, H. Ko, H. Lee, S. G. Lee and K. Cho, *J. Mater. Chem. A*, 2016, **4**, 15522–15535.
50 A. Levitsky, S. A. Schneider, E. Rabkin, M. F. Toney and G. L. Frey, *Mater. Horiz.*, 2021, **8**, 1272–1285.
51 C. McDowell, M. Abdelsamie, M. F. Toney and G. C. Bazan, *Adv. Mater.*, 2018, **30**, 1707114.
52 M. Ghasemi, N. Balar, Z. Peng, H. Hu, Y. Qin, T. Kim, J. J. Rech, M. Bidwell, W. Mask, I. McCulloch, W. You, A. Amassian, C. Risko, B. T. O'Connor and H. Ade, *Nat. Mater.*, 2021, **20**, 525–532.

